

Imaging elastodynamic and hydraulic properties of in-situ fractured rock: An experimental investigation exploring effects of dynamic stressing and shearing

C. Wood¹, P. Shokouhi², P. Manoghara²ⁿ, J. Rivière², D. Elsworth^{3,1}, C. Marone¹

¹Dept. of Geosciences, Pennsylvania State University, University Park, PA 16802, USA

²Dept. of Engineering Science and Mechanics, Pennsylvania State University, University Park, PA 16802, USA

³Department of Energy and Mineral Engineering, EMS Energy Institute, and G3 Center, The Pennsylvania State University, University Park, PA, USA

Key Points:

- enter point 1 here
 - enter point 2 here
 - enter point 3 here

Abstract

We describe laboratory experiments to elucidate the relationship between nonlinear elasticity and permeability evolution in fractured media subjected to local stress perturbations. This study is part of an effort to image fluid pathways and fracture properties using active-source acoustic monitoring during fluid injection and shear of rough fractures. Experiments were conducted with L-shaped samples of Westerly granite fractured in-situ under tri-axial conditions with deionized water subsequently circulated through the resulting fractures. After in-situ fracturing, we separately imposed oscillations of the applied normal stress and pore pressure with amplitudes ranging from 0.2 to 1 MPa and frequencies from 0.1 to 40 Hz. During these dynamic perturbations an array of piezoelectric transducers continuously transmitted ultrasonic pulses across the fracture to monitor the evolving elastic response. We interpret the resulting evolution of elastic wave properties in the context of elastic nonlinearity and relate the estimated nonlinearity parameters to the relative change in permeability of the fractured media. Fracture roughness is then altered in-situ by shearing, with the generation of breccia and wear products. We document the evolution of permeability and fracture contact stiffness as a function of dynamic stressing and shear offset and discuss our findings in relation to fractures in Earth's crust.

Plain Language Summary

[enter your Plain Language Summary here or delete this section]

1 Introduction

Dynamic stresses associated with energy production and waste water sequestration (injection, pumping, and transport of supercritical H_2O-CO_2 fluids) are a potentially important contributor to injection-induced seismicity [Healy et al., 1968; Raleigh et al., 1976; Simpson et al., 1988; Sminchak and Gupta, 2003; McNamara et al., 2015; McGarr et al., 2015; Walsh and Zoback, 2015]. These perturbations can cause significant changes in the local stress field and poromechanical properties in the subsurface and therefore act as a diagnostic for impending fault reactivation and prospective changes in permeability - among other utilities. Therefore, it is crucial to understand how fluid injection influences the hydromechanical properties of rocks and, in particular, associated fractures. Natural and anthropogenic sources of dynamic perturbation each impact porome-

46 mechanical properties through similar mechanisms and in similar ways, suggesting uniform
47 controls relating nonlinear stiffness to poromechanical properties. We characterize these
48 dependencies to define the potential to link nonlinear acoustic properties to the evolution
49 of reservoir state and behavior.

50 Empirical evidence from the field and laboratory show that earthquakes and subsequent seismic waves cause transient changes in rock stiffness in the proximity of faults.
51 Specifically, field observations document a sudden reduction in elastic wave velocity associated with co-seismic softening and a post-seismic recovery of rock stiffness that is logarithmic in time [e.g., Brenquier et al., 2008]. Similar observations have been made in
52 the laboratory [Elkhouri et al., 2014]. Moreover, lab studies using dynamic acousto-elastic
53 testing [Shokouhi et al., 2017], show that ultrasonic wave velocity decreases during dynamic stressing and then recovers with the logarithm of time. These studies show that
54 dynamic strains on the order of 10^{-6} are sufficient to cause the nonlinear elastic effects
55 [Rivière et al., 2015]. We have performed careful laboratory experiments to investigate
56 the connection between fluid flow and elastic nonlinearity (i.e. the stress-dependency of
57 elastic wave velocity and amplitude) of fractured rock.

58 Nonlinear elastic response is sensitive to many fracture properties: geometry, flow
59 pathways, asperity compliance, and friction. Currently, the literature characterizing relationships
60 between elastodynamic and poromechanical response and subsequent recovery is limited [Shokouhi et al., 2019]. We present results from sophisticated and highly-constrained
61 laboratory experiments in which we combine the analysis of nonlinear elastodynamic and hydraulic data.

62 The nonlinear behavior of rocks is sensitive to both fine-scale features and second-order
63 constitutive effects, such as fracture apertures (impacting flow pathways, asperity stiffness) and nonlinear stiffnesses (impacted by rate-dependent friction and healing).
64 In order to fully understand the ramifications of dynamic stressing in the subsurface, we
65 need elucidate the relationship between the elastodynamic and hydro-mechanical properties
66 of fractured rocks.

67 In this paper we build on prior work [Shokouhi et al., 2019] to image acoustic nonlinearity across a fracture using multiple PZT receivers. Also, we relate the average nonlinear acoustic response to fracture permeability as an averaged hydraulic measurement.
68 Another important parameter that we analyze is how the fracture recovers from dy-

78 namic stressing. Furthermore, we investigate the effect of shearing on our results, repli-
79 cating complex natural fractures with heterogeneous roughness and gouge.

80 2 Experimental Setup

81 We conducted laboratory experiments in a true triaxial configuration using frac-
82 tured granite samples in-situ while simultaneously measuring flow rate and nonlinear elas-
83 tic properties. Samples of Westerly granite were cut into L-shape blocks (69 x 45 50 x
84 26 mm, Figure 1) with 3 mm deep notches on the top and base to guide the evolution
85 of planar fractures driven by shear loading to failure. The L-shape is used for maintain-
86 ing constant nominal contact area during both initial fracture then shear. Our samples
87 were saturated with deionized water and then placed between steel loading platens with
88 embedded piezoelectric transducers. The P-polarized lead-zirconate transducers (PZTs)
89 from APC International Ltd. are 6.5 mm in diameter, with a center frequency of 500 kHz.
90 The PZTs are epoxied in blind holes 4 mm from the rock sample (Figure 1). The load-
91 ing platens contain internal conduits to provide a line source of fluid at either end of the
92 fracture plane. Fluid access at both ends of the fracture was via a narrow channel (45
93 x 1 mm) fitted with sintered porous fits (permeability 10^{-14} m^2) and fed by five 1.6-
94 mm diameter holes. Deionized water was pumped through the fracture at constant pres-
95 sure drop using independent high speed servo-controllers for both inlet and outlet pres-
96 sure (Figure 1).

97 The experimental apparatus consists of a stiff load frame and two hydraulic pis-
98 tons capable of applying force in either displacement- or load-control mode and a pres-
99 sure vessel with independent control of pore and confining pressures. Applied forces are
100 measured using custom-built, beryllium-copper strain-gauge load cells mounted on each
101 loading piston. The load cells have an amplified output of $\pm 5 \text{ V}$ with an accuracy of ± 5
102 N and are calibrated with a Morehouse proving-ring. Displacements are measured with
103 direct-current displacement transducers (DCDT), with an accuracy of $\pm 0.1 \mu\text{m}$. Con-
104 fining pressure was created using a food-grade heat transfer oil (XCELTERM 600, Radco
105 Industries). A linear variable differential transformer was attached to the sample inside
106 the pressure vessel to accurately ($\pm 0.1 \mu\text{m}$) measure changes in fracture aperture. Pres-
107 sure intensifiers fitted with LVDTs and pressure transducers were used to control the con-
108 fining pressure and the internal upstream and downstream fluid pressures.

109 Each axis of loading is independently servo-controlled and all stresses, strains, fluid
 110 pressures and fluid volumes were recorded with a ± 10 V, 16-channel 24-bit analog-to-digital converter at 10 kHz and averaged to sampling rates of 100 Hz or 1 kHz. Fluid
 111 flow across the fracture was measured using upstream and downstream pore-pressure intensifiers and the permeability was subsequently calculated. Active ultrasonic data were
 112 recorded using a VantageTM Research Ultrasound (Verasonics) system. We use broad-
 113 band (0.02-2 MHz) PZTs (APC International Ltd. 6.35 diameter compressional crys-
 114 tals), which were successively pulsed every 1 ms on the transmitting side and recorded
 115 at the receiver side with a sampling rate of 25 MHz. The input signal is a half sine with
 116 a frequency of 500 kHz. Also, a pulse from the Verasonics system accompanied the PZT
 117 excitation and was recorded by the 24-bit analog-to-digital data acquisition system. This
 118 provided a means for synchronizing the fast-sampled “ultrasonic” and lower sampled “poro-
 119 mechanical” data. We used these data to measure changes in the permeability and elas-
 120 ticity of the fractured rock samples.
 121

122 Before commencing each experiment, the samples were installed in the pressure ves-
 123 sel then filled with confining fluid before a horizontal stress of 20 MPa was applied. Con-
 124 fining fluid pressure was slowly increased to 15 MPa afterwards. We then applied pore
 125 pressure: inlet ($P_{pA} = 4$ MPa) and outlet ($P_{pB} = 2$ MPa). At this point there was ef-
 126 fectively no flow because the Westerly granite matrix permeability is very low ($< 10^{-20} m^2$)
 127 and the confining fluid pressure is greater than the pore pressure (we confirmed no flow
 128 between sample and jacket). Once all fluid pressures and solid stresses were applied, the
 129 ultrasonic data acquisition was started. The sample was then fractured in-situ by increas-
 130 ing the shear stress at constant normal stress. After fracturing of the sample we locked
 131 the vertical piston (no displacement allowed) and executed the dynamic stressing pro-
 132 tocol illustrated in Figure 2a while making continuous measurements of fluid flow and
 133 ultrasonic properties.
 134

135 After executing a series of normal stress and pore pressure oscillation protocols,
 136 the fractured sample was sheared twice in 4 mm increments (for a total of 8 mm). Dur-
 137 ing shear, acoustic emissions (AEs) were monitored (passive source recording). Subse-
 138 quent to each shearing step the dynamic stressing protocol was repeated. We incorpo-
 139 rated shearing in this investigation to determine its influence on both the nonlinear elas-
 140 tic and flow properties of the fracture. The fracture aperture is changed through shear,
 141 in effect, mimicking the complexity of fractured subsurface rock.

142 **2.1 Experimental Procedure**

143 Each experiment commenced with extensive sample preparation in which the West-
 144 erly granite was cut and notched, sealed in a latex jacket, and then placed inside the pres-
 145 sure vessel. After sealing the pressure vessel and loading the sample, inlet and outlet flow
 146 ports were pressurized to 4 MPa and 2 MPa, respectively. At this stage there was no flow
 147 because the Westerly granite matrix permeability is very low ($< 10^{-20} \text{ m}^2$) and the con-
 148 fining fluid pressure (around the jacketed sample) is much larger than the pore pressure,
 149 preventing the short-circuiting flow of water around the sample. A shear load was then
 150 applied with the vertical piston in displacement mode at a constant rate of $10 \mu\text{m/s}$. Sam-
 151 ples fractured in-situ after reaching a critical stress of $\approx 55 \text{ MPa}$, after which we locked
 152 the vertical piston. Fluid flow and acoustic emissions were measured during fracture, but
 153 here we focus on dynamic stressing which was implemented via oscillations of the effec-
 154 tive normal stress.

155 Oscillations of the applied normal stress were applied with the horizontal loading
 156 piston at prescribed amplitudes (0.2 to 3 MPa) and frequencies (0.1, 1, 10, 40 Hz). Pore
 157 pressure oscillations were achieved by oscillating P_{PA} while holding P_{PB} constant at am-
 158 plitudes of 0.2 to 3 MPa and frequencies of 0.1, 1, 10 Hz. Multiple sets of normal stress
 159 and pore pressure oscillations of varying amplitudes and frequencies were applied to in-
 160 vestigate: (1) repeatability and direct comparison between the two modulated stresses
 161 (normal stress and pore pressure) and (2) amplitude and frequency dependencies of the
 162 measured response. Post-fracture dynamic stressing is plotted in Figure 3d (highlighted
 163 in yellow) and shows the normal stress (red) and pore pressure (blue) oscillations. To
 164 investigate the effect of shearing and resulting changes in fracture aperture and gener-
 165 ated wear material on elastic nonlinearity and permeability, the sample was sheared in
 166 two 4 mm (held at $\sigma_{NS} = 20 \text{ MPa}$), stages. After each shearing stage the oscillation pro-
 167 tocol was applied to the sample. Initially, the in-situ fracture was quite rough with fines
 168 throughout, but the effect of shear reduces and changes this roughness; the old contacts
 169 were broken and new contacts formed, changing the extent to which the two halves of
 170 the fracture were mated. Throughout shear the size, shape, and amount of wear prod-
 171 ucts, or fines, continuously evolves and likely has a complicated effect on fluid flow. These
 172 measurements allow investigation of how fracture aperture is related to the elastodynamic
 173 and hydromechanical properties.

174 **2.2 Permeability Measurements**

175 We measured flow rates independently at the fracture inlet (Q_A) and outlet (Q_B)
 176 using the outputs of LVDTs on the pressure intensifiers. After verifying the steady state
 177 flow condition ($Q_A - Q_B \leq 5\%$), Darcy's law was used to calculate permeability k :

$$k = \frac{\mu L}{S} \frac{Q}{\Delta P_P} \quad (1)$$

178 where $Q = \frac{1}{2}(Q_A + Q_B)$ is the average flow rate ($\frac{m^3}{s}$), μ is the fluid viscosity ($10^{-3} Pa \cdot$
 179 s) at $20^\circ C$, L is the flow path given by the length of the sample (50 mm) and S is the
 180 cross sectional area perpendicular to the flow path ($45 \times 26 mm^2$). Specifically, k is the
 181 bulk permeability, that is, the permeability of the surrounding rock matrix (on order of
 182 $10^{-21} m^2$) and of the fracture. Alternative calculations of permeability are valid [Zhang
 183 et al., 2017; Ishibashi et al., 2018], however we are interested in relative changes in per-
 184 meability in response to dynamic stressing, rather than the absolute value of fracture
 185 permeability.

186 **2.3 Ultrasonic Measurements: Active Source**

187 Ultrasonic waves transmitted through the fracture were recorded continuously in
 188 each experiment. Half-cycle sinusoidal pulses with an amplitude of 40 V and center fre-
 189 quency of 500 kHz were emitted consecutively from each transmitting transducer (9 piezo-
 190 electric discs arranged in a 3 x 3 matrix embedded within the right-hand loading platen
 191 in Figure 1b) with a pulse repetition frequency of 100 Hz or 1000 Hz during the low and
 192 high frequency (≥ 10 Hz) stress oscillations, respectively. The waveforms were ampli-
 193 fied (~ 40 dB) and recorded for all the receiving transducers (12 piezoelectric discs ar-
 194 ranged in a 4 x 3 matrix embedded within the left-hand loading platen in Figure 1b).
 195 In this study we utilized 1 transmitter and 3 receivers.

196 **3 Results**

197 We combine ultrasonic data, strain measurements, and permeability to document
 198 the nonlinear elastodynamic response and poromechanical effects of dynamic stressing.
 199 Here, we draw from an extensive set (~ 10) of experiments, calibrations, and tests to fo-
 200 cus on data from two distinct experiments with a range of stressing amplitudes and fre-
 201 quencies.

202 **3.1 Nonlinear elastodynamic and hydraulic responses**

203 Linear elasticity does not adequately describe the behaviour of rocks. Even undam-
 204 aged rocks exhibit a range of nonlinearity due to a variety of structural features such as
 205 microcracks and soft grain boundaries (Rivière et al., 2015). When fractured or dam-
 206 aged, the nonlinearity of the rock is further affected by contact acoustic nonlinearity at
 207 fracture interfaces. The characteristic responses to dynamic stressing (transient soften-
 208 ing, velocity modulation, and slow recovery) as shown in Figure 5, are indicative of non-
 209 linear mesoscopic elasticity (Guyer and Johnson, 2009) and highly informative on rock
 210 microstructure, fractures, and intergrain contacts. Crucially, these are the features that
 211 also control the hydraulic properties of rock.

212 Through our active source ultrasonic monitoring we characterize the elastodynamic
 213 properties of the fractured Westerly granite by quantifying its response to dynamic stress-
 214 ing. Figure 5 demonstrates typical recorded elastodynamic and hydraulic responses to
 215 a 1 Hz, 1 MPa normal stress oscillation in experiment p4966. We characterize the elas-
 216 todynamic response with three parameters to describe the nonlinearity, $\Delta c/c_0$, dc/c_0 ,
 217 and $\Delta A/A_0$. We observe steady-state wave velocity c_0 before dynamic stressing which
 218 causes an immediate reduction followed by a further transient decrease. Wave velocity
 219 recovers to a new steady-state value that we quantify as Δc . The RMS wave amplitude
 220 is calculated in the time domain in a window comprising the first arrived p-wave, related
 221 to fracture stiffness. Dynamic stress oscillations result in a sudden decrease in amplitude
 222 relative to the initial value A_0 to a new temporary non-equilibrium state. Therefore, both
 223 $\Delta c/c_0$ and $\Delta A/A_0$ represent nonlinear ratios that demonstrate the transient effect of dy-
 224 namic loading on fracture stiffness, for a range of stress amplitudes and frequencies. Al-
 225 though RMS amplitude can be extracted from our data, that is not the main focus of
 226 this paper, but some results are reported in the Supplemental Materials. Another non-

linearity parameter that we identify is modulation of the wave velocity, dc , during oscillations at frequencies that are harmonics of the driving frequency. This quantity represents the average amplitude of wave velocity modulations during dynamic perturbations after the system reaches a non-equilibrium steady-state. Finally, after being stressed, the fractured rock exhibits long-term “recovery” trending toward the initial c_0 value, in which the wave velocity or amplitude evolves to a new steady state. The wave velocity evolution from post-oscillation to initial c_0 is well described by a logarithmic function of the form $c = p_1 \log t + p_2$, where p_1 is the slope (recovery rate) \dot{c} and p_2 is the intercept.

We also measure the evolution of permeability due to dynamic stressing and correlate it with nonlinear elasticity. In our experiments, elastic waves propagate orthogonal to the fracture plane and their amplitude, phase and speed depend on the fracture stiffness that is modulated by aperture. Hydraulic measurements, comparing inlet and outlet fluid flow across the fracture plane, tell a similar story; permeability and transmissivity reveal changes in fracture aperture. The stress-induced changes in permeability are captured by two parameters: (1) The transient change in permeability $\Delta k/k_0$ defined as the %-change due to the imposed normal stress or pore pressure oscillations, normalized by the pre-oscillation permeability k_0 as illustrated in Figure 5c [Candela et al., 2014] and (2) the logarithmic rate of permeability recovery after the transient increase \dot{k} where $k = q_1 \log t + q_2$, where q_1 is the slope (recovery rate) and q_2 is the intercept. Figure 5 shows the pre-oscillation permeability k_0 and the post-oscillation permeability $k = k_0 + \Delta k$ calculated by averaging the measured values over 10- and 1-s time windows. Calculation discontinuities in permeability measurements shown in Figure ?? correspond to times for which inlet/outlet flow rate difference exceeds the 5% threshold that we impose to ensure steady state flow. Permeability during dynamic stressing is indeterminate because there is no steady-state flow and the diffusion time across the fracture is slower than the higher oscillation frequencies (10 and 40 Hz).

To better illustrate how the elastodynamic and hydraulic properties of fractured rock change in response to dynamic perturbation we show an excerpt from the post-fracture stage of experiment p4975 in Figure 7. Figure 7 demonstrates how the inlet and outlet flow rates evolve during a 0.1 Hz normal stress oscillation; three colorbars highlight zoomed cycles in Figure ???. Note the clear evidence of compression and tension in the fracture normal displacement with increased and decreased normal stress (Figure 7). The inlet

260 Q_A flow rate is in phase with the imposed stressing, but the outlet flow Q_B is 180 out
261 of phase and of a much smaller magnitude than that of the inlet; furthermore, the am-
262 plitude trends are modulated throughout the oscillation. For sufficiently long duration
263 stressing the wave velocity modulations reach a steady-state. These observations demon-
264 strate the magnitude of changes we are characterizing and also reinforce that the frac-
265 ture is continuously evolving during the dynamic perturbations; contacts undergo com-
266 pression and tension resulting in changing fluid flow paths along the fracture.

267 In subsequent subsections we discuss how nonlinear elastodynamic and hydraulic
268 parameters $\Delta c/c_0$, $\Delta k/k_0$, dc/c_0 , and $\Delta A/A_0$ vary with normal stress and pore pressure
269 oscillation amplitudes and frequencies. We also discuss how these results are affected by
270 shearing for both experiments p4966 and p4975.

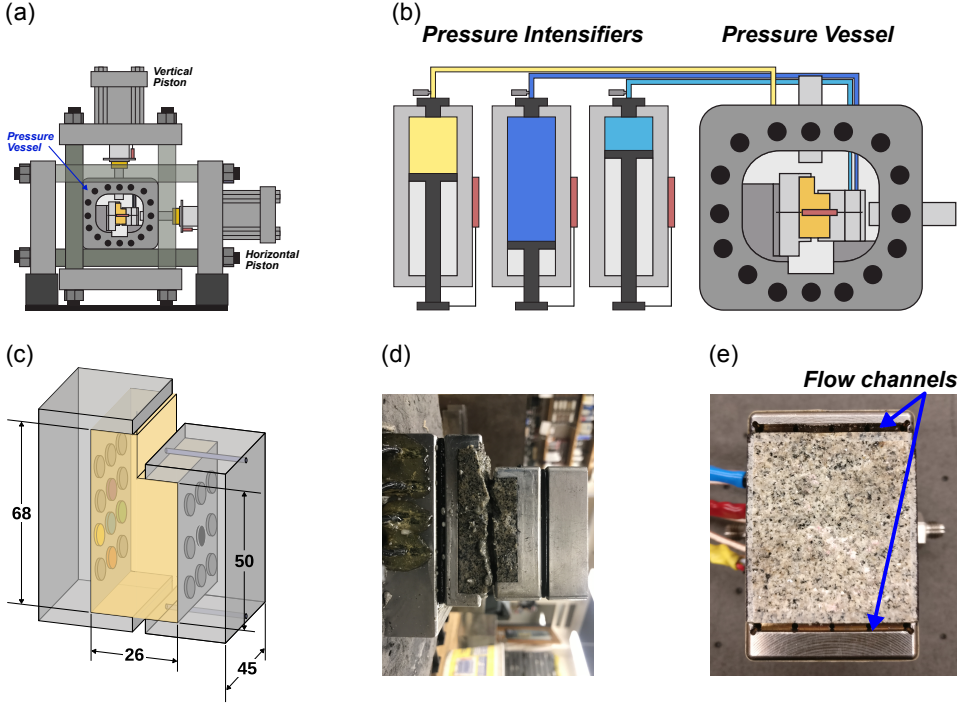


Figure 1. (a) Experiments were conducted in the Penn State Rock and Sediment Mechanics laboratory using the Biaxial Deformation Apparatus (Biax). The Biax has servo-controlled vertical and horizontal pistons and a 10 kHz 24-bit analog to digital data recorder. (b) A pressure vessel is inserted into the Biax to create true triaxial loading. Pressure intensifiers control the confining pressure (P_C) and sample (P_{PA} and P_{PB}) fluid pressures. (c) L-shaped samples of granite were loaded with platens containing piezoelectric transducers (p-polarized). The shorter platen has internal conduits to provide fluid at each end of the fracture plane via narrow channels (45×1 mm). Each channel is covered by a sintered porous frit (permeability $\sim 10^{-14} \text{ m}^2$) and fed by five 1.6 mm diameter holes. The frits ensure homogeneous fluid distribution at each end of the fracture. After securing the sample in the loading platens it is sealed in a latex jacket to separate confining and pore fluids. (d) A photo of the sample after experimentation highlights the degree of roughness resulting from the in-situ fracturing. (e) Post mortem photograph showing the rough fracture and fluid flow channels.

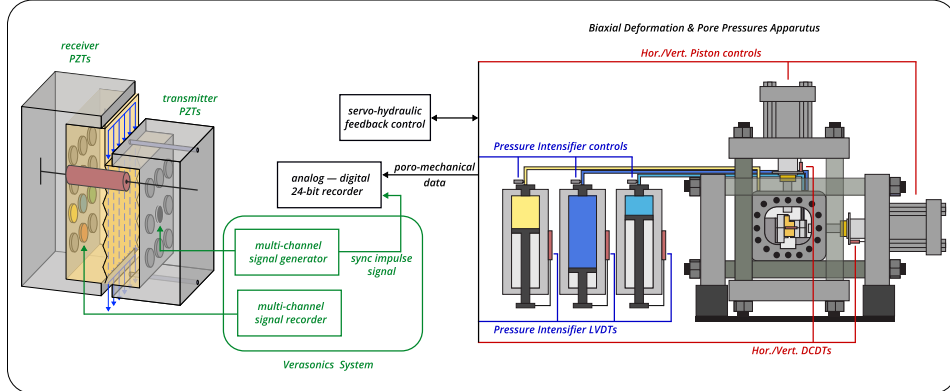


Figure 2. Schematic of the single direct shear configuration with the block diagram showing the main features of the data acquisition system for both the poro-mechanical and ultrasonic data. The Biax consists of two hydraulic pistons capable of applying vertical and horizontal loads in displacement or load control. Forces are measured using custom-built strain-gauge load cells mounted on the displacement rams. The load cells have an amplified output of 5 V with an accuracy of 5 N and are calibrated with a Morehouse proving-ring. Displacements are measured with direct-current displacement transducers (DCDT), with an accuracy of $\pm 0.1\mu m$. Each axis of loading is independently servo-controlled and all stresses, strains, fluid pressures and fluid volumes were recorded with ± 10 V, 16-channel 24-bit analog-to-digital converters at 10 kHz and averaged to sampling rates of 100 Hz or 1 kHz. Fracture permeability was measured using upstream and downstream pore-pressure intensifiers. Active ultrasonic data were recorded using a Vantage TM Research Ultrasound (Verasonics) system. We use broadband (0.02-2 MHz) PZTs (APC International Ltd. 6.35 mm diameter compressional crystals), which were successively pulsed every 1 ms on the transmitting side and the recording rate at the receiver side was 25 MHz. The input signal is a half sine with a frequency of 500 kHz. Also, a pulse from the Verasonics system accompanied the PZT excitation and is recorded by the 24-bit analog-to-digital data acquisition system. This allows synchronizing of the ultrasonic data to the poro-mechanical data and then their joint analysis to measure changes in the permeability and elasticity of the fractured rock samples, explained more fully in the signal analysis procedure.

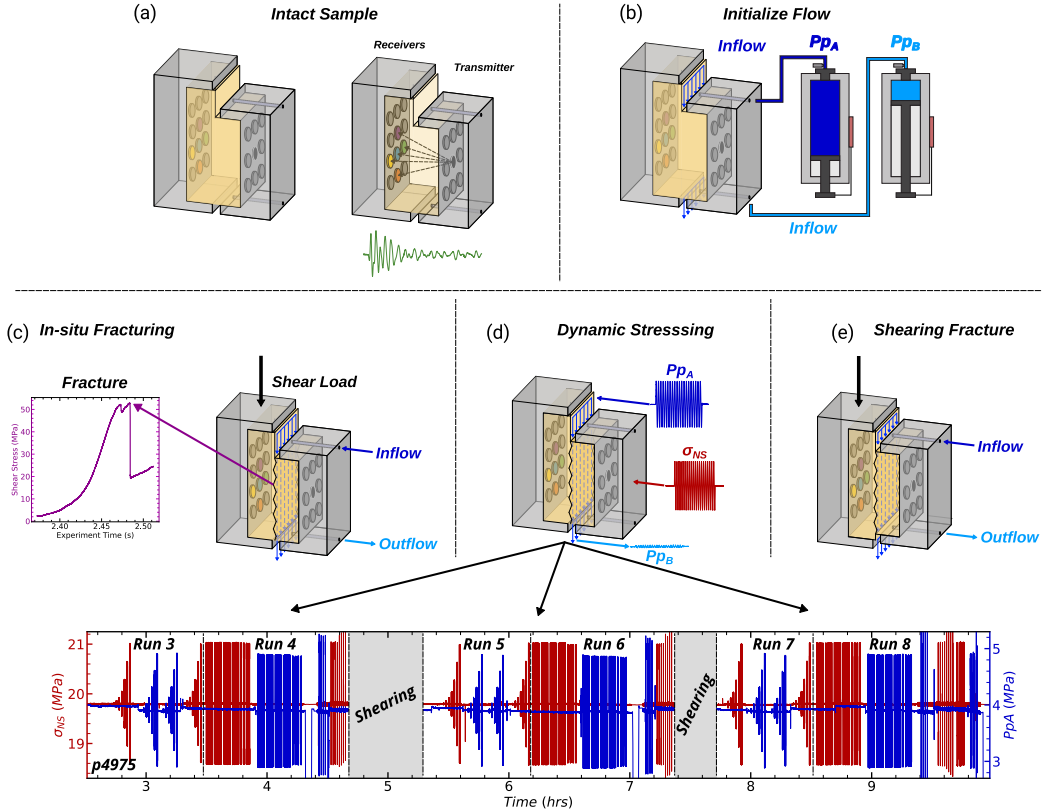


Figure 3. (a) Sketch showing sample dimensions and approximate PZT transmitter - receiver ray paths. (b) Fluid flow and pore pressure with inlet ($P_{PA} = 4$ MPa) and outlet ($P_{PB} = 2$ MPa). (c) Shear stress on the fracture plane was increased by advancing the long end of the L-shaped sample at a constant rate of $10 \mu\text{m}/\text{s}$ while holding the short end in place. Fracture occurred in two stages at ≈ 55 MPa. (d) Sketch showing the oscillation protocol applied to the freshly fractured sample. Multiple sets of P_P and σ_{NS} oscillations of varying amplitude (up to about ± 1 MPa) and frequency (0.1, 1, 10 and 40 Hz) were applied. (e) Fractures were sheared in two stages, each followed by the dynamic stressing protocol.

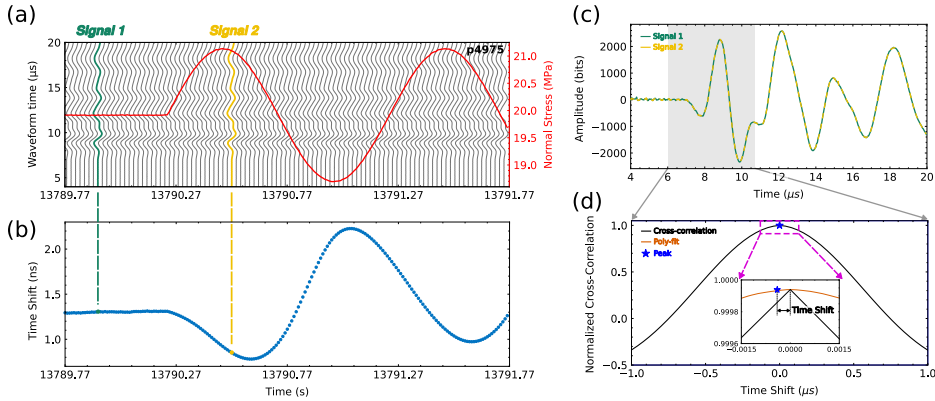


Figure 4. (a) Excerpt from Run 4 of experiment p4966 (see Fig. 3 for context in p4975) shows part of a 1 Hz, 1 MPa normal stress oscillation (red) and the concurrent raw ultrasonic waveforms (grey). The number of waveforms in the waterfall plot has been decimated for clarity. (b) Time shift was calculated by cross-correlating the waveforms with a reference waveform. (c) An example of a reference, unperturbed, waveform (green) and perturbed waveform (dashed yellow) highlights the similarity. (d) The maximum linear correlation between the reference and perturbed waveforms from cross-correlation is used to determine the time shift. The inset shows improvement of time shift calculations with a 2nd order polynomial fitting procedure.

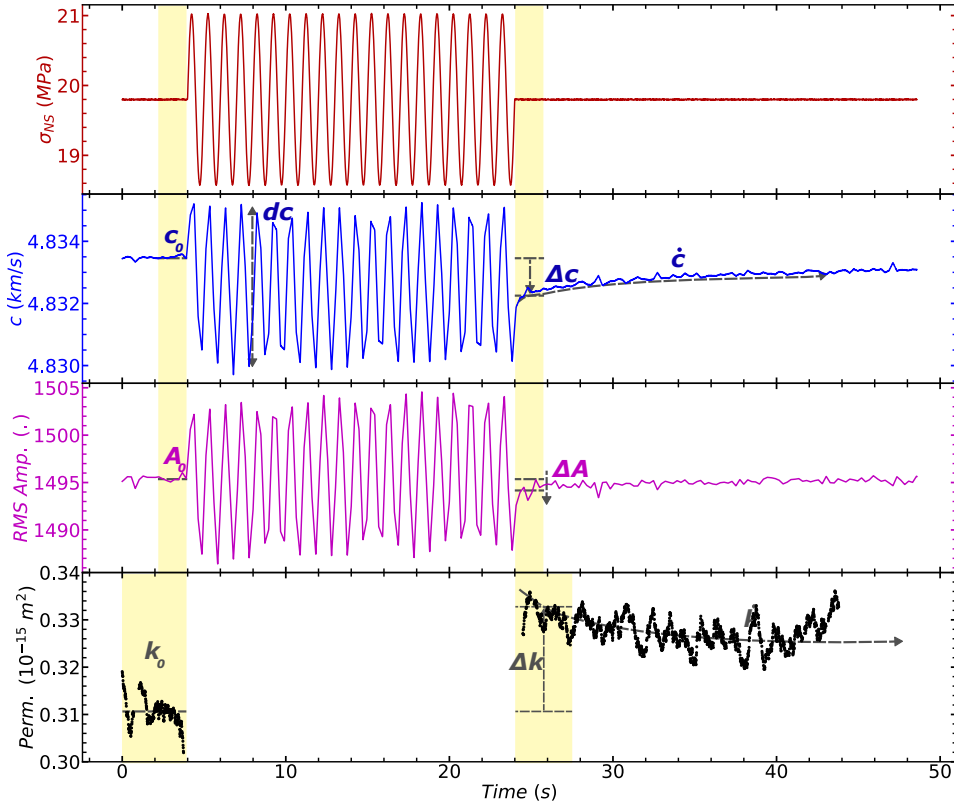


Figure 5. Details of elastodynamic and hydraulic response to dynamic stress oscillation, see Run 4 of p4975 in Fig. 3. Wave velocity and permeability changes are calculated using the measured values before and after oscillations averaged over the time windows indicated by yellow boxes. Permeability measurements are shown only for steady state flow when the inlet/outlet flow rates differ by < 5%. We measure the dynamically induced changes in p-wave velocity (\dot{c}) and permeability (\dot{k}) as well as their changes Δc and ΔA relative to the initial values c_0 and A_0 . Furthermore, we measure the average change in p-wave velocity during dynamic stressing oscillations as dc .

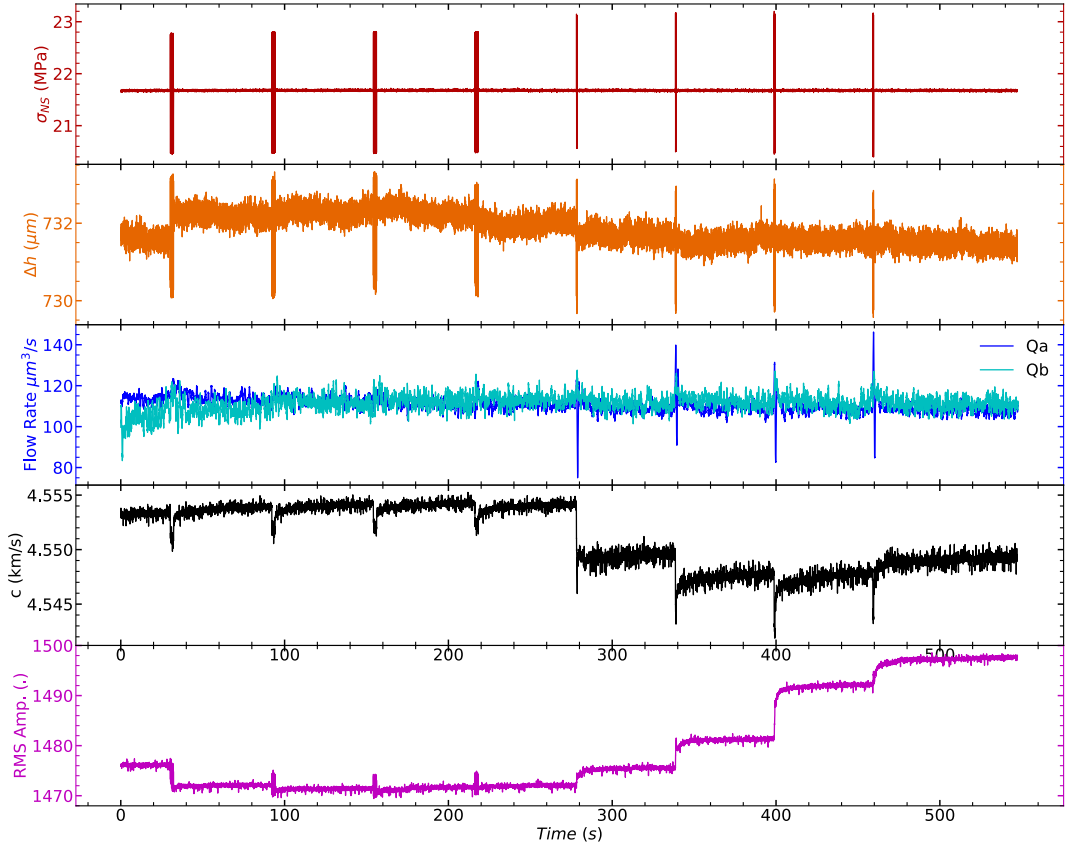


Figure 6. Elastodynamic and hydraulic data for one full dynamic stressing protocol with pore pressure oscillation (See Fig. 3: Run 4 experiment p4975. These data are for a ray path from the center transmitter to the blue receiver in Figure 2. Two sets of 1-MPa amplitude pore fluid pressure oscillations were imposed at frequencies of 0.1, 1, 10 and 40 Hz. In all cases p-wave velocity shows a transient reduction upon dynamic stressing followed by recovery. Oscillations begin with a pore pressure increase and thus fracture aperture Δh increases initially, as effective stress drops, and then undergoes a transient change that varies with stressing history. Wave amplitude also shows a complex response to stress oscillations including both transient and long term changes.

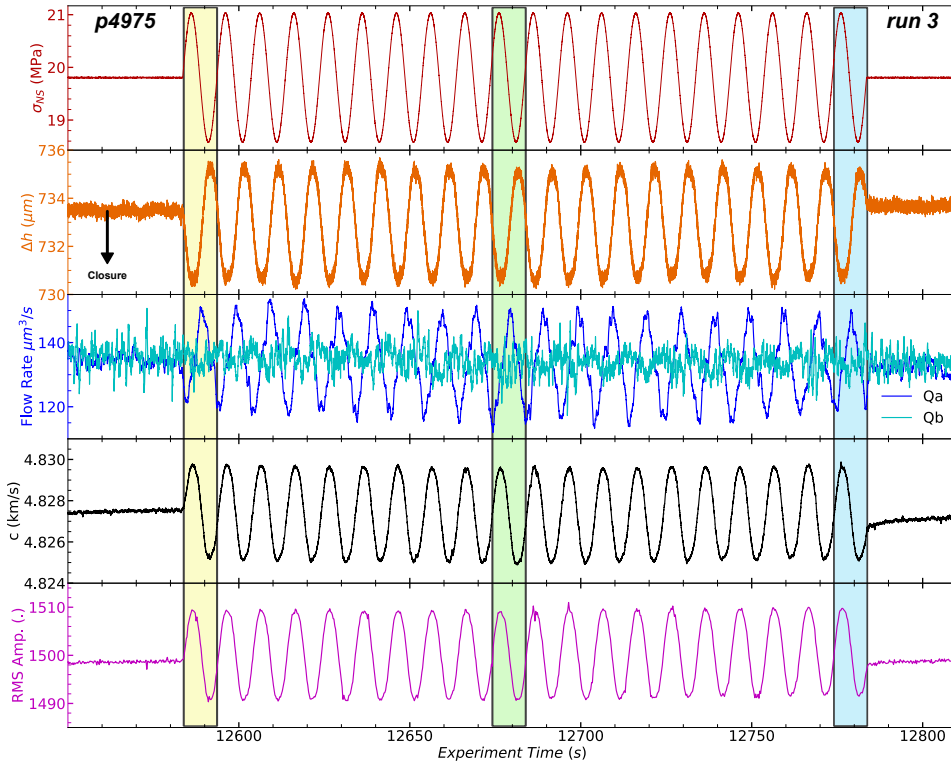


Figure 7. Elastodynamic and hydraulic data for one set of applied normal stress oscillations at a frequency of 0.1 Hz and amplitude of 1 MPa (See Fig. 3). Fracture aperture decreases initially as normal stress increases and then varies in phase with fracture normal stress. Fluid flow data from the fracture inlet (PpA) and outlet (PpB) document the transient response to changes in fracture aperture and stress state. Note that inflow is phase lagged relative to fracture aperture. Elastic wave speed and amplitude are shown for the direct path pair (center transmitter to blue receiver in Figure 2). Three sections are highlighted showing one full cycle in the beginning, middle, and end of the normal stress oscillation.

271 **3.2 Dynamic Stress-induced Changes in Permeability and Wave Veloc-**
 272 **ity**

273 One hypothesis driving our work is that transient elastic softening and nonlinear
 274 elasticity can provide information about rock fracture properties via dynamic stressing.
 275 A corollary is that changes in fracture aperture cause both changes in permeability and
 276 elasticity. A more complete understanding of both physical phenomena is important for
 277 understanding processes that control energy production from, and waste storage in, the
 278 subsurface. In this section, we report and compare the stress amplitude and frequency
 279 dependencies for both sets of parameters.

280 The dependency of $\Delta k/k_0$ on the amplitude of normal stress and pore pressure os-
 281 cillations is shown in Figure 8, which additionally differentiates the order in which the
 282 1 Hz oscillations sets were imposed. We observe in experiments p4966 and p4975 fairly
 283 similar $\Delta k/k_0$ results for the post-fracture case. This is not entirely surprising because,
 284 although these experiments pertain to different samples/fractures, both samples are West-
 285 erly granite and the same loading conditions were used to produce approximately pla-
 286 nar fractures resulting in presumably similar apertures and amounts of fragmentation.
 287 Interestingly, this similarity deteriorates especially for pore pressure oscillations after the
 288 first shear phase of the experiments. After shearing the fractures (5 mm in p4966 and
 289 4 mm in p4975) fragmented wear products develop at the interface, which inevitably com-
 290 plicated flow – clogging and unclogging during the pore pressure oscillations such that
 291 wear material was dislodged from certain parts of the fracture or lodged in other parts.

292 Compared to dynamic stressing via pore pressure, permeability $\Delta k/k_0$ is relatively
 293 unaffected by oscillations of the applied normal stress oscillations for post-shear cases.
 294 This suggests that gouge material generated during shear is not mobilized to the degree
 295 it is by pore pressure, perhaps because pore fluids are more effective in moving gouge
 296 material and clogging/unclogging flow paths. This mechanism is not fully understood
 297 but likely plays a significant role in this complicated process.

298 We observe that the relative permeability change $\Delta k/k_0$ generally scales with the
 299 amplitude of the 1 Hz normal stress oscillation post fracture and pore pressure oscilla-
 300 tions and that the order in which oscillations were applied have an effect on the perme-
 301 ability enhancement. There are cases especially for post-shear oscillations where small
 302 oscillation amplitudes ($< 0.5\text{ MPa}$) result in a modest reduction in permeability for nor-

303 mal stress oscillations, but can result in relatively larger reductions for Pore pressure os-
304 cillations. Despite scatter, fairly similar relationships are observed for the two separate
305 experiments.

306 The sequenced order of oscillations does not necessarily correlate to a specific per-
307 meability enhancement or reduction, but does have an effect on the overall results. This
308 is most likely due to the fact that the pore pressure and normal stress oscillations do not
309 strictly alternate, although the order is consistent in post-fracture, post-shear 1, and post-
310 shear 2 parts of the experiments as shown in (reference your protocol).

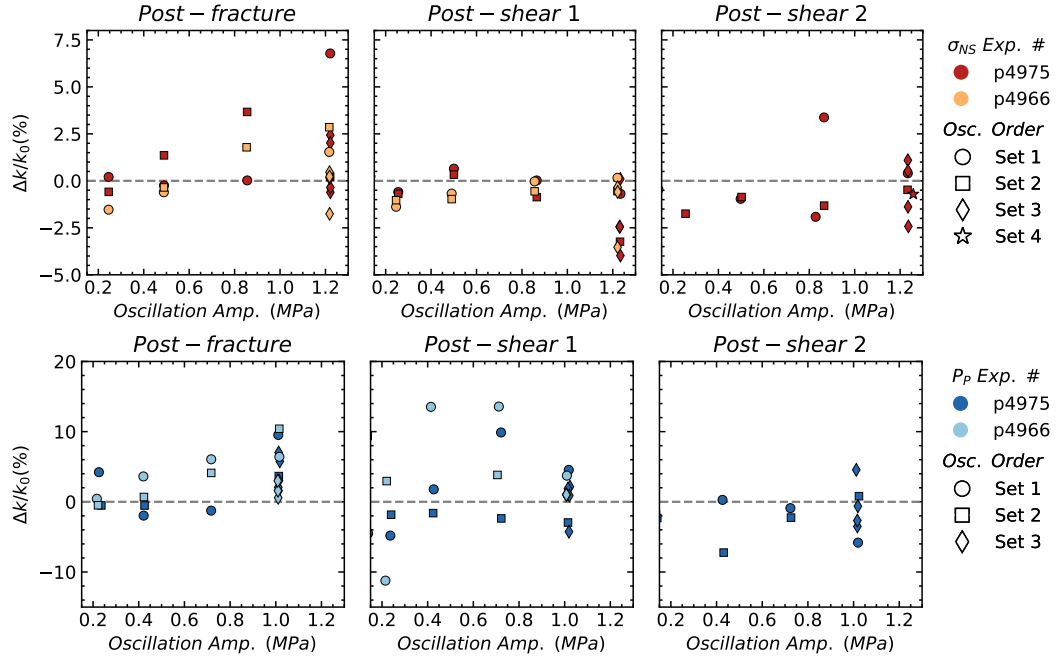


Figure 8. Relative changes in permeability for dynamic stressing via applied normal stress (top row) σ_{NS} and pore pressure (lower row) P_p at 1 Hz. Data are shown for the period just after the fracture formed (post-fracture) and after each increment of shear. Comparing post-fracture results to post-shear we observe a general reduction of permeability enhancement via dynamic stressing with smaller values of $\Delta k/k_0$. Gouge generated from shear is likely clogging flow pathways along the fracture plane. The hypothesized impediment to flow for the post-shear oscillation sets causes a reduction in permeability enhancement, especially for the post-shear 2 oscillation set.

311 The relative change in velocity $\Delta c/c_0$ for the direct transmitter-receiver pair as a
312 function of 1 Hz normal stress and pore pressure oscillation amplitudes are plotted in
313 Figure 9. As expected [Rivière et. al, 2015], we observe increasing nonlinearity (more
314 negative $\Delta c/c_0$) with oscillation amplitude for both normal stress and pore pressure.

315 In this measure of fracture nonlinearity there is a clearer trend between oscillation
316 order and magnitude, for this transmitter-receiver path. Normal stress oscillations for
317 the post-fracture case exhibit less nonlinearity compared to subsequent oscillation sets. The
318 degree of nonlinearity from pore pressure oscillations, though linear with oscillation am-
319 plitude, remains relatively unchanged with shearing.

320 The effect of shear on fracture nonlinearity is more obvious for pore pressure os-
321 cillations and rather scattered for applied normal stress oscillation sets. Interestingly,
322 the nonlinearity relationship with amplitude barely changes with amount of shear for p4975;
323 though for p4966, shearing the fracture increases the nonlinearity. However, for applied
324 normal stress, successive shear scatters the trend we observe in post-fracture sets, pre-
325 sumably deriving from dramatic changes in asperity contacts that occur with progres-
326 sive shear displacement.

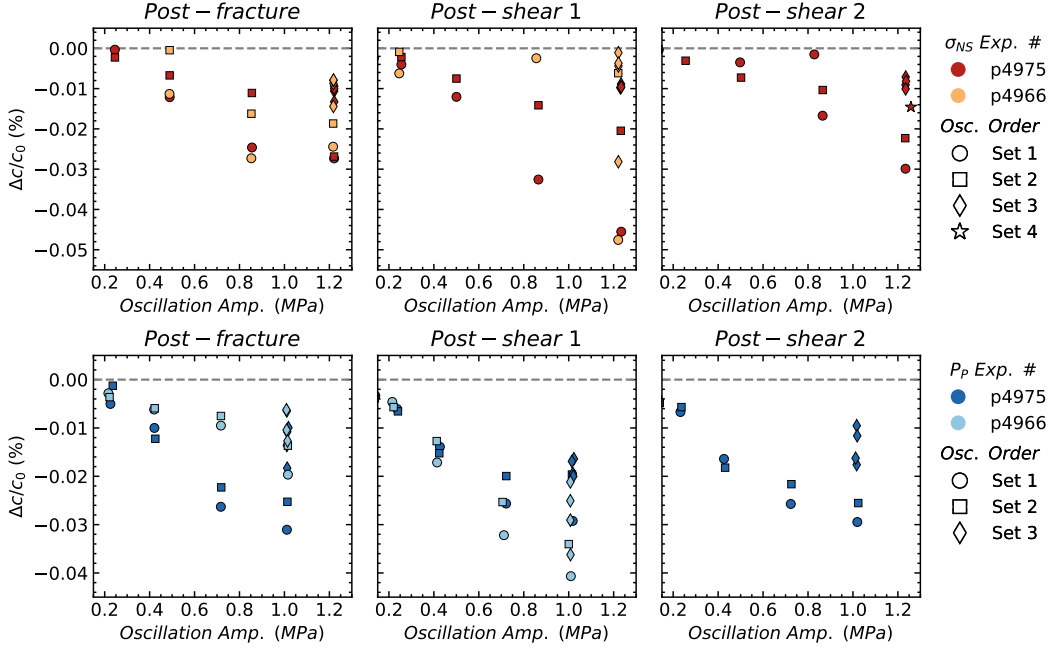


Figure 9. Relative changes in p-wave speed for dynamic stressing via applied normal stress (top row) σ_{NS} and pore pressure (lower row) P_p . Data are shown for the direct transmitter-receiver pair (see Figure 2). Note that the magnitude of Δc increases as a function of oscillation amplitude. Transitioning from post-fracture results to post-shear results, we observe decreased and more scattered nonlinearity.

327 3.3 Spatial Variations of the Nonlinear Elastodynamic Response

328 The elastic response ($\Delta c/c_0$) presented in Figure 9 corresponded to a single pair
 329 of transducers. Figure 10 shows a coarse view of the nonlinear elastodynamic response
 330 across the fracture as a function of applied oscillation amplitude. Note that data point
 331 shape corresponds to oscillation frequencies. The direct path sensor, blue PZT in Fig-
 332 ures 10 – 11) shows a general trend of increasing nonlinearity with stress oscillation am-
 333 plitude and frequency, in both experiments. The other sensors measure more scatter and
 334 also more linearity in the case of the bottom sensor of p4975. The shearing reduces non-
 335 linearity (direct pair) and modestly increases nonlinearity (top sensor path), but does
 336 not have an overall coherent trend for both experiments and all increments of shear. The
 337 response to pore pressure oscillations, Figure 11, shows more coherent results as com-
 338 pared to applied normal stress. Again, there is a general trend in increasing nonlineari-
 339 ty with amplitude and oscillation frequency; it is interesting that the bottom receiver
 340 path exhibits markedly lower nonlinearity. Furthermore, there is much more similarity
 341 in results for the separate experiments than observed in the normal stress oscillations.
 342 Another important observation is that shearing has little effect on the magnitude of non-
 343 linearity for pore pressure oscillations.

344 The scatter in these results is not unexpected given that the fracture has a hetero-
 345 geneous aperture and irregularly distributed wear products, especially following the ap-
 346 plication of shear displacement. It is conceivable that shear increases the aperture in some
 347 locations, which could be filled with wear/gouge material or remain empty, while other
 348 parts of the fracture aperture could be closed. These possibilities may be partially re-
 349 sponsible for the complicated behavior we observe.

350 To further our understanding of the coupling between elastodynamic and hydraulic
 351 response to dynamic stressing, we investigate the spatial variations of the elastic response
 352 along the fracture by analyzing all available transmitter-receiver pairs measurement of
 353 wave velocity (Figures 10 – 11). Figure 12 relates permeability changes $\Delta k/k_0$, an hy-
 354 draulic measurement averaged over the fracture plane, to the change in wave velocity
 355 $\Delta c/c_0$ averaged across all receiver locations. The data point shapes again correspond to
 356 the oscillation frequencies and their sizes correspond to oscillation amplitude. The main
 357 observation for the post-fracture oscillation sets is that relative changes in permeabil-
 358 ity and wave velocity are correlated. That is to say, larger normal stress or pore pres-

359 sure oscillation amplitudes and frequencies produce larger transient softening and per-
360 meability enhancement. Overall, shear weakens this relationship, reducing the amount
361 of nonlinearity and permeability enhancement for both methods of dynamic stressing.
362 Though, in the case of normal stress oscillations, the relationship with amplitude and
363 frequency still exists, but the overall slope decreases due to shear displacement.

364 We conjecture that the nature of the correspondence between nonlinear elastody-
365 namic and hydraulic properties of fractured rock depend not only on fracture aperture
366 change due to stressing but also on clogging mechanisms. During both types of dynamic
367 stressing fracture flow conduits are likely to be clogged/unclogged in a complicated fash-
368 ion, resulting in mobilization of gouge material (generated from in-situ fracture and sub-
369 sequent shear displacement) and permeability enhancement/reduction. This has also been
370 observed in previous studies of Berea sandstone (Elkhoury et al., 2011; Candela et al.,
371 2014, 2015). However unlike in previously reported studies, we observe permeability en-
372 hancement for both normal stress and pore pressure oscillations (for amplitudes > 0.5
373 MPa). Thus, fracture aperture change from stressing and clogging mechanisms can not
374 adequately explain the rich underlying physics.

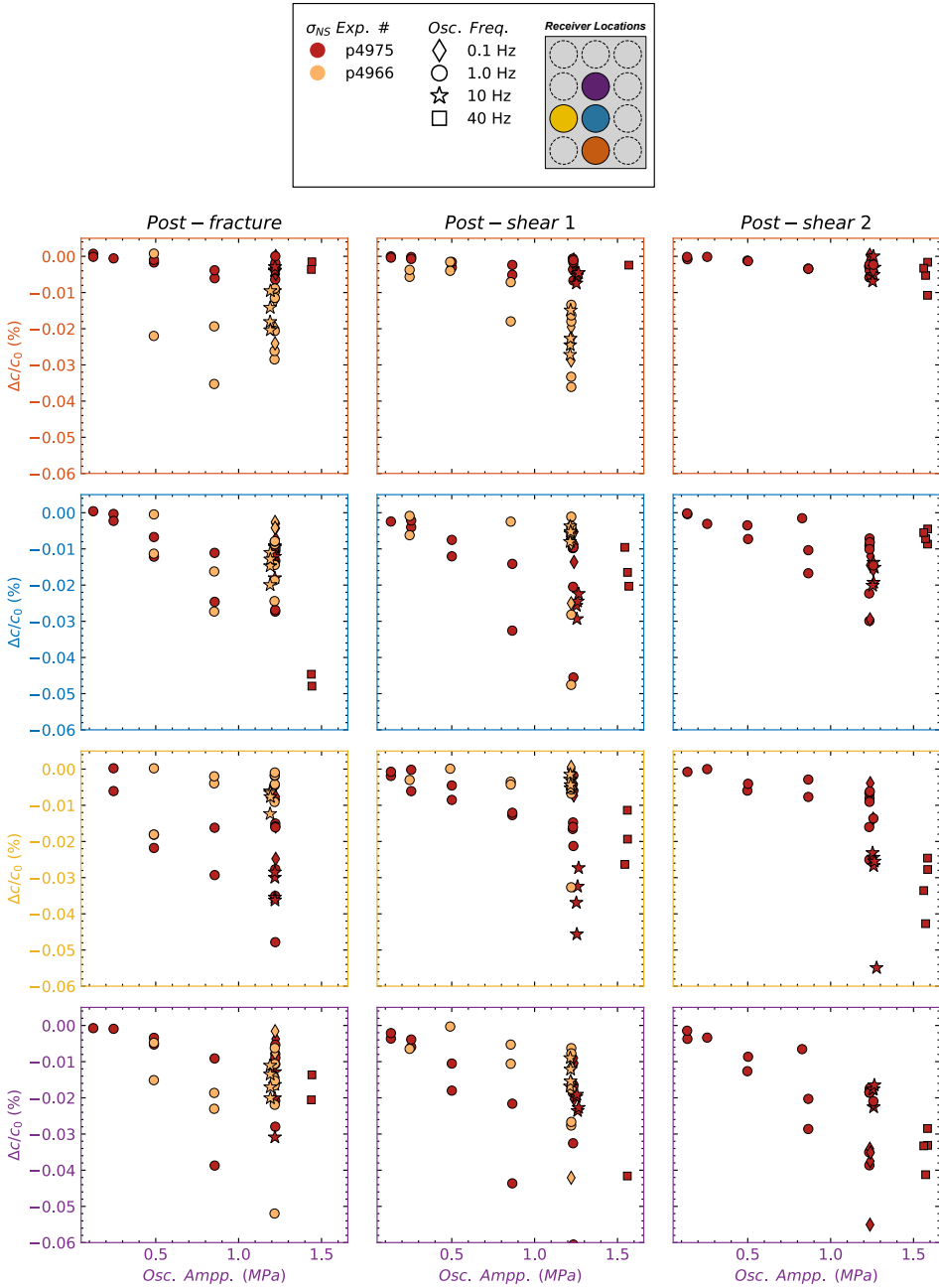


Figure 10. Nonlinearity as a function of σ_{NS} oscillation amplitude for each receiver. Transitioning from post-fracture results to post-shear results, we observe decreasing nonlinearity. The plot colors correspond to PZT receiver locations. These results demonstrate the spatial variability in nonlinear elasticity across the fracture plane and furthermore shows that the two Westerly granite samples exhibit similar responses to the normal stress oscillations.

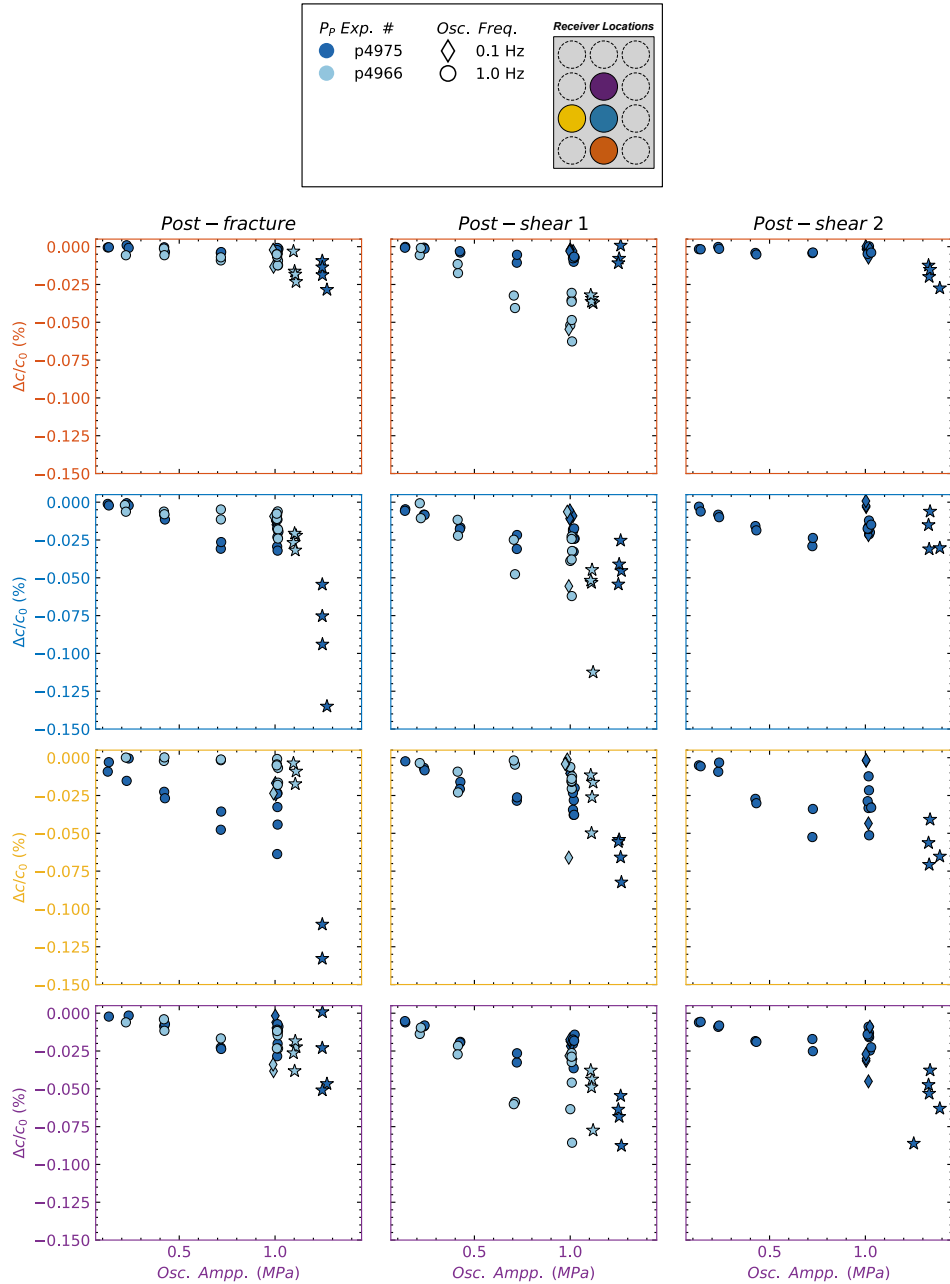


Figure 11. Nonlinearity as a function of pore pressure oscillation amplitude for each receiver.

Transitioning from post-fracture results to post-shear results, we observe decreased nonlinearity. The spatial variability shows that the pore pressure oscillations in some of the receiver locations throughout the experiments cause larger changes in elastic nonlinearity than the normal stress oscillations.

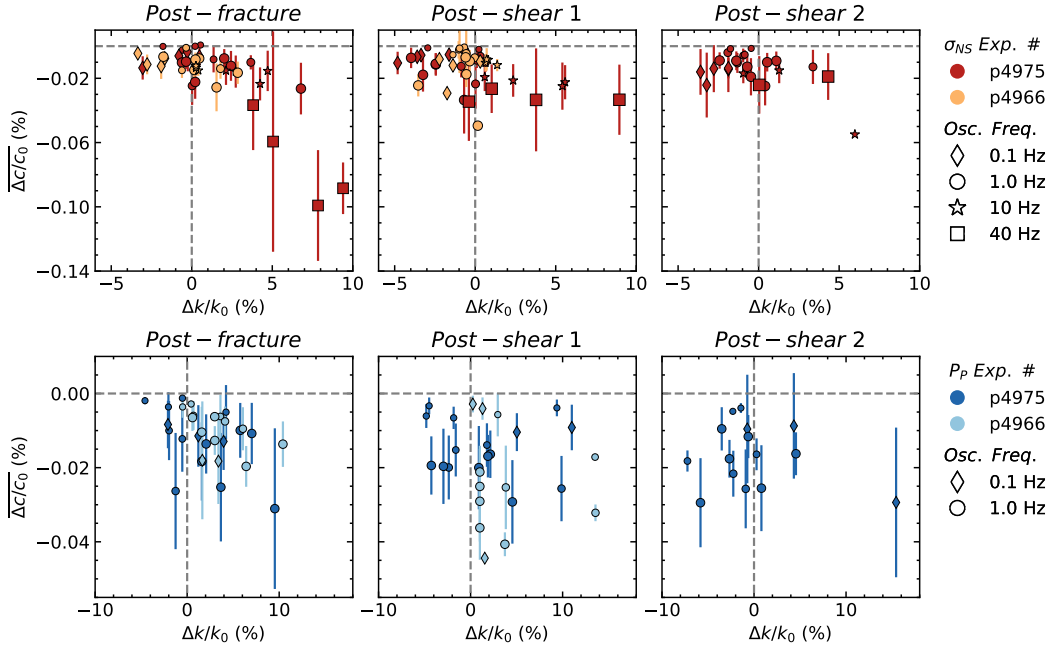


Figure 12. Nonlinearity as a function of permeability change for σ_{NS} and P_P oscillations averaged over all receivers. Data point shapes correspond to the oscillation frequencies and their sizes to amplitude. In post-fracture oscillation sets, relative changes in permeability and wave velocity are correlated. That is to say, larger normal stress or Pore pressure oscillation amplitude and frequencies produce larger transient softening and permeability enhancement. Overall, shear weakens this relationship, reducing the amount of nonlinearity and permeability enhancement for both methods of dynamic stressing.

375 **3.4 Wave Velocity Modulation**

376 The direct effect of dynamic stressing is an instantaneous modulation in wave ve-
 377 locity at harmonic frequencies of the driving frequency. We denote the mean velocity am-
 378 plitude as dc (e.g., Figure 5). The relative change in average velocity oscillations dc/c_0
 379 is a proxy for the nonlinear parameter β , estimated from the second harmonic (e.g., [Rivière
 380 et al., 2013, 2015]). We observe a monotonic relationship between the magnitude of dc/c_0
 381 and oscillation amplitude for both rock samples (Figure 13).

382 There is a consistent trend that subsequent oscillation sets decrease the magnitude
 383 of nonlinearity of dc/c_0 for normal stress modulation. Pore pressure oscillations exhibit
 384 little to no change through subsequent repetitions, except for larger driving amplitudes.
 385 Shearing the fracture decreases the measured nonlinearity, especially for experiment p4966
 386 (Figure 15). This is also observed for pore pressure oscillations in sample p4966, but p4975
 387 exhibits little to no change in dc/c_0 nonlinearity after the first shear increment. Then,
 388 after the second shear, pore pressure oscillations interestingly increase the nonlinearity.
 389 We posit that the two types of dynamic stressing activate two different mechanisms: (1)
 390 opening/closing of pore throats from normal stress oscillations and (2) directly dislodg-
 391 ing and mobilizing fines along the fracture from pore pressure oscillations. This is con-
 392 sistent with our observations of other nonlinearity parameters.

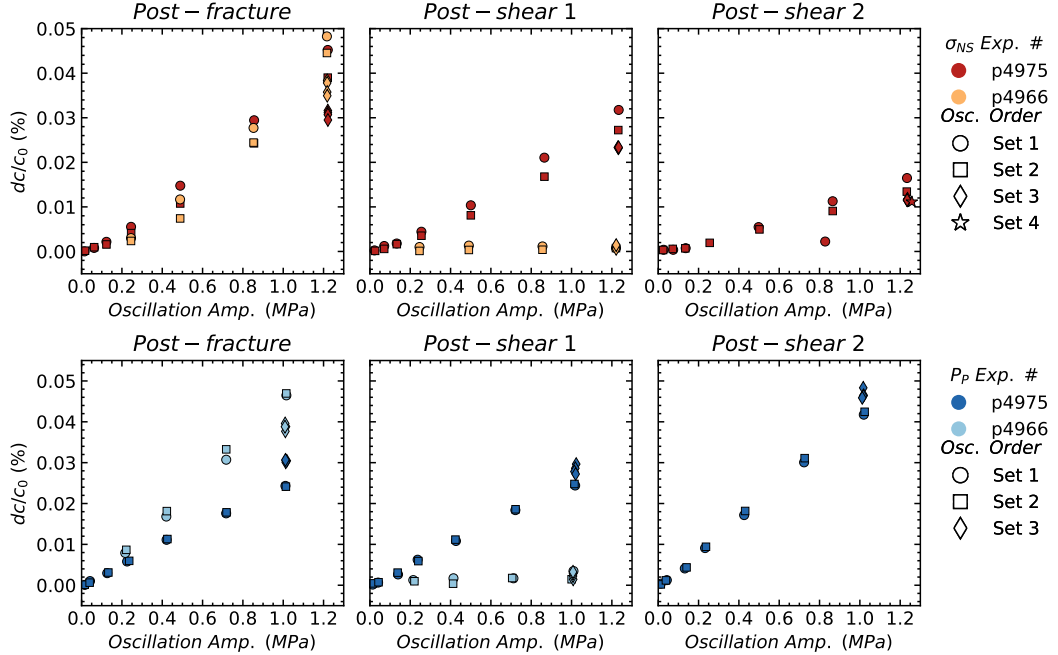


Figure 13. Velocity amplitude modulation averaged over all receivers (dc/c_0) as a function of normal stress and Pore pressure oscillations. There is a systematic reduction in dc/c_0 with accumulated shear for normal stress oscillations and there is very little variation in the oscillation order. The results from pore pressure oscillations in p4966 tell a similar story as the normal stress oscillations, but the pore pressure oscillations in p4975 show no change from post-fracture to post-shear 1 and an increase in dc/c_0 from post-shear 1 to 2.

3.5 Permeability and Wave Velocity Recovery from Dynamic Stressing

The long term evolution of permeability and wave velocity reveal the extent to which fines are transported along the fracture and how fracture asperities recover from dynamic stresses. We observe trends, particularly in experiment p4975, where the slope of the permeability recovery linearly decreases with pore pressure oscillations (see insets of Figure 14). Permeability recovery is generally less correlated with normal stress oscillation amplitude. These results suggest that the opening and closing mechanism of the fracture from normal stress oscillations is not very effective in unclogging fines to migrate along the fracture. Large amplitude pore pressure oscillations are more effective in mobilizing the fines, thus allowing for a more rapid recovery to its initial state. Furthermore, there is little effect of order of oscillation for both stimulation methods.

Shearing the fracture does not result in a systematic modulation to permeability recovery after normal stress oscillations, but results in slower permeability recovery rates in response to pore pressure oscillations, see Post - Shear 1 and 2 from Figure 14. This suggests that normal stress oscillations (opening and closing of pore throats) become less effective in mobilizing fines and the fracture asperities are permanently damaged/ altered, so the permeability does recover to the initial pre-oscillation state. Because there is an increase in the accumulation of fines from shearing, the permeability recovers slower in response to pore pressure oscillations. We posit that the wear material is comminuted as a result of subsequent shearing and normal stress oscillations, is transported along the fracture during the pore pressure oscillations, and impedes a recovery from the transient change.

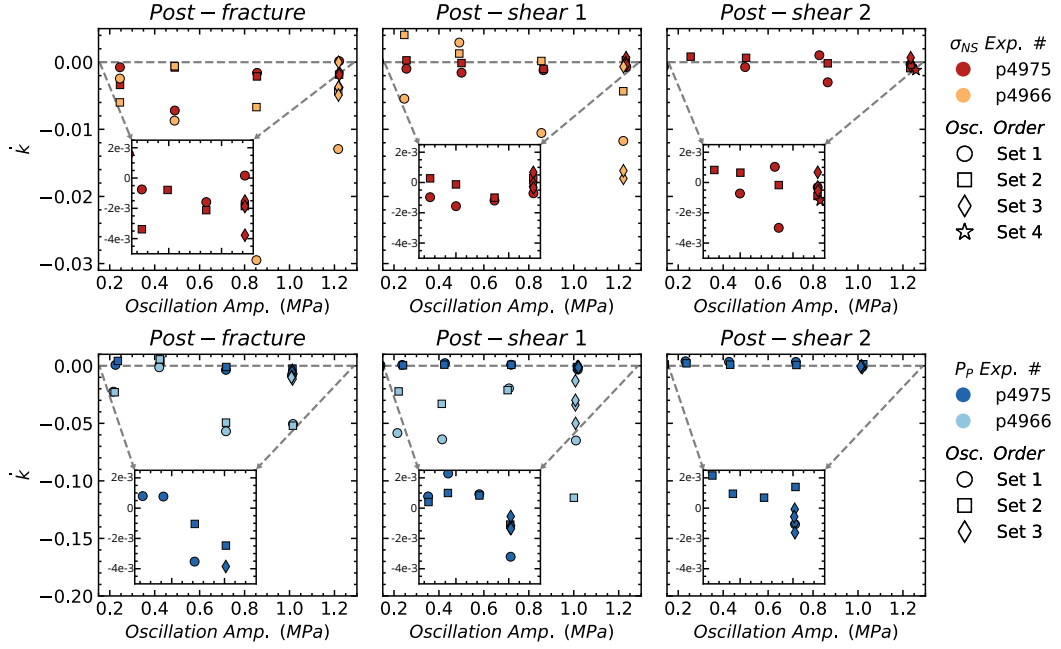


Figure 14. Permeability recovery \dot{k} as a function of applied stress oscillations for σ_{NS} and P_P . Data point shapes indicate oscillation order. Recovery rate \dot{k} linearly decreases with P_P oscillation amplitude in p4975, but is not correlated with both σ_{NS} oscillation amplitude. Furthermore, subsequent shearing results in slower \dot{k} for P_P oscillations.

415 The wave velocity recovery rate \dot{c} for the direct transmitter-receiver pair as a func-
416 tion of 1 Hz normal stress and pore pressure oscillation amplitudes are plotted in Fig-
417 ure 15. We observe faster recovery with oscillation amplitude for both normal stress and
418 pore pressure. In the post-fracture phase, there is a noticeable effect of order of σ_{NS} os-
419 cillations on recovery rate; later oscillations exhibit smaller magnitude of \dot{c} , which demon-
420 strates detectable damage to the fracture asperities from the first oscillation set.

421 The effect of shear on fracture \dot{c} is a decrease in the magnitude of recovery rate and
422 a flattening of the relationship between \dot{c} and oscillation amplitude for both perturba-
423 tion methods. There is perhaps a complex effect from deformation of fracture asperities
424 and the granular wear material that inhibit the recovery from the transient response to
425 dynamic stressing.

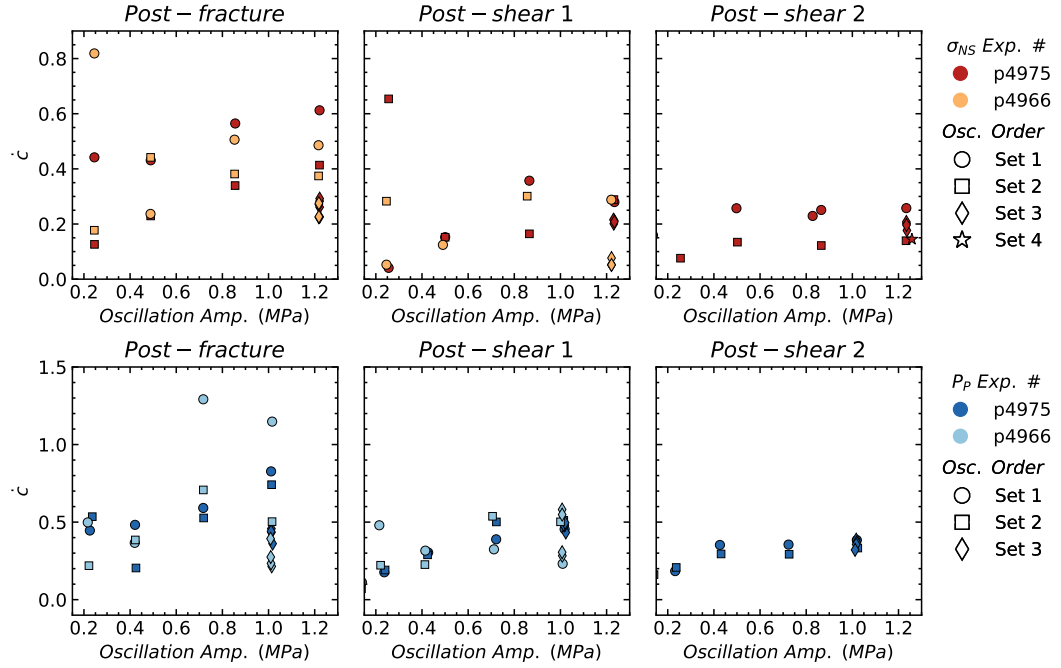


Figure 15. Wave velocity recovery \dot{c} for direct-path receiver as a function of applied stress oscillations for σ_{NS} and P_P . Data point shapes represent oscillation order. The recovery rate \dot{c} modestly increases with both σ_{NS} and P_P . Shearing decreases \dot{c} and flattens after the second shear displacement.

426 Figure 16 relates the wave velocity recovery rate \dot{c} averaged over all receiver loca-
427 tions to permeability changes \dot{k} , a hydraulic measurement across the fracture. The main
428 observation \dot{c} and \dot{k} are mostly uncorrelated for normal stress oscillations, but are more
429 correlated for pore pressure oscillations in the post-fracture phase. Also, there does not
430 seem to be obvious scaling of frequency with the the relation between \dot{c} and \dot{k} . Overall,
431 shearing the fracture decreases both the velocity and permeability recovery rates for pore
432 pressure oscillations, especially in experiment p4975.

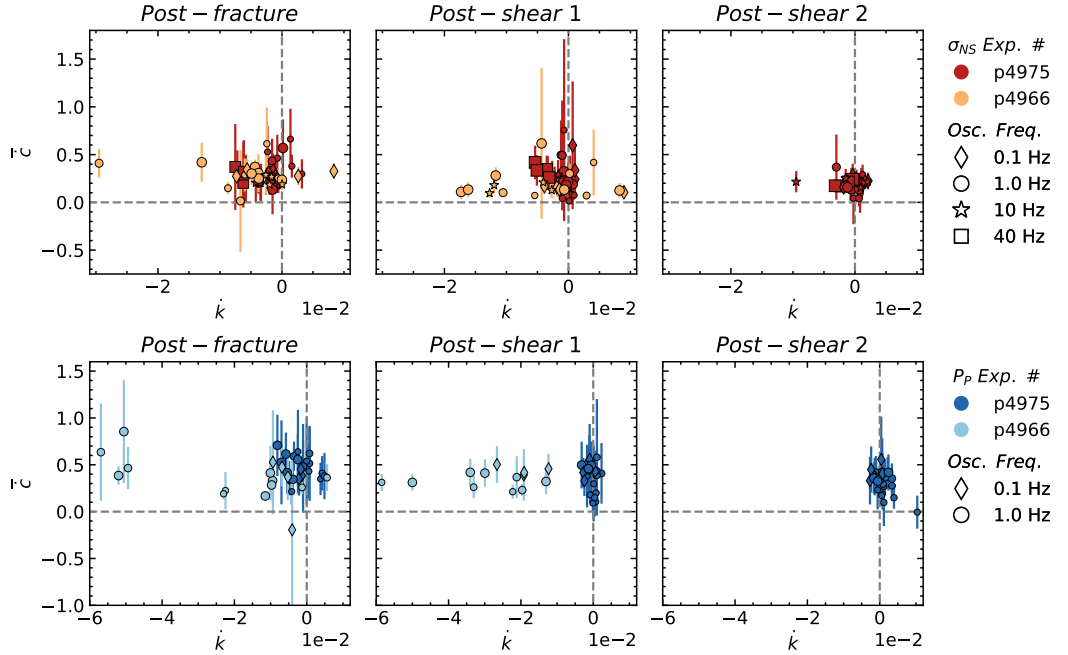


Figure 16. Wave velocity recovery rate \dot{c} as a function of permeability recovery rate \dot{k} for σ_{NS} and P_P oscillations averaged over all receivers. Data symbol shapes correspond to the oscillation frequencies and their sizes to amplitude. In post-fracture oscillation sets, both high frequency and large amplitude oscillations yield faster recovery rates for both velocity and permeability. The predominant effect of shearing is a significant reduction in \dot{k} for σ_{NS} oscillations, but increase for P_P oscillations.

433 **4 Conclusions**

434 We report laboratory experiments to determine the effects of dynamic stressing and
 435 shearing on elastodynamic and hydraulic properties of fractured rock. Processes controlling
 436 fluid flow in reservoirs, including subsurface waste disposal, and hydrocarbon pro-
 437 duction derive from a complex interplay of these properties. Monitoring in-situ fractures
 438 with active source ultrasonic transmission and fluid permeability during dynamic stress-
 439 ing driven by both total stresses and fluid pressures reveals the complex relation between
 440 elastodynamic and hydraulic properties.

441 In response to oscillations of effective normal stress, Westerly granite samples ex-
 442 hibit characteristic transient softening, acoustic velocity fluctuations, and slow recovery,
 443 informing us about microstructure and contact mechanics. We observe that large am-
 444 plitude and high frequency oscillations generally increase permeability, with pore pres-
 445 sure oscillations producing the largest enhancement of permeability. Furthermore, we
 446 document spatial variability in elastodynamic properties across the fractures, revealing
 447 the effect of variations in fracture aperture and contact stiffness. Shearing generally de-
 448 creases this nonlinearity parameter for both oscillation modes. The exact underlying physics
 449 remain unclear of how fracture asperity and aperture changes resulting from dynamic
 450 stressing and clogging mechanisms account for these results. However, our observations
 451 do suggest that the two types of dynamic stressing activate two different mechanisms;
 452 aperture change dominates during applied normal stress oscillations and unclogging dom-
 453 inates during pore pressure oscillations.

454 Future experiments with pre-fractured samples will include characterization of sur-
 455 face roughness with high-resolution profilometry to better constrain the underlying me-
 456 chanics of aperture and permeability change. Furthermore, we will develop methods to
 457 collect fine gouge material generated from in-situ fracturing and shearing in the down-
 458 stream pore pressure lines in an attempt to quantify the degree to which unclogging mech-
 459 anisms are responsible for the results we observe.

460 **Acknowledgments**

461 Experimental and data analysis assistance from Benjamin Madara and Jiang Jin, respect-

462 fully, was invaluable. Technical assistance from Steven Swavely is gratefully acknowledged.

463 This study was supported by .

464 **References**